

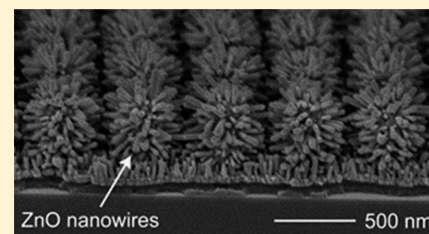
# Wicking Enhancement in Three-Dimensional Hierarchical Nanostructures

Zhiting Wang,<sup>†</sup> Junjie Zhao,<sup>‡</sup> Abhijeet Bagal,<sup>†</sup> Erinn C. Dandley,<sup>‡</sup> Christopher J. Oldham,<sup>‡</sup> Tiegang Fang,<sup>†</sup> Gregory N. Parsons,<sup>‡</sup> and Chih-Hao Chang<sup>\*,†</sup>

<sup>†</sup>Department of Mechanical and Aerospace Engineering and <sup>‡</sup>Department of Chemical and Biomolecular Engineering, North Carolina State University, Raleigh, North Carolina 27695, United States

## Supporting Information

**ABSTRACT:** Wicking, the absorption of liquid into narrow spaces without the assistance of external forces, has drawn much attention due to its potential applications in many engineering fields. Increasing surface roughness using micro/nanostructures can improve capillary action to enhance wicking. However, reducing the structure length scale can also result in significant viscous forces to impede wicking. In this work, we demonstrate enhanced wicking dynamics by using nanostructures with three-dimensional (3D) hierarchical features to increase the surface area while mitigating the obstruction of liquid flow. The proposed structures were engineered using a combination of interference lithography and hydrothermal synthesis of ZnO nanowires, where structures at two length scales were independently designed to control wicking behavior. The fabricated hierarchical 3D structures were tested for water and ethanol wicking properties, demonstrating improved wicking dynamics with intermediate nanowire lengths. The experimental data agree with the derived fluid model based on the balance of capillary and viscous forces. The hierarchical wicking structures can be potentially used in applications in water harvesting surfaces, microfluidics, and integrated heat exchangers.



## INTRODUCTION

The wicking of fluids in micro/nanostructures<sup>1–22</sup> is an interesting physical phenomenon and has many potential applications in thermal management,<sup>7–10</sup> moisture harvesting,<sup>11–15</sup> and biomedical devices.<sup>16–18</sup> In these materials, the wicking behavior varies according to the fluid properties, the surface treatment, and the structural geometry. In early work nearly one hundred years ago, before the term “wicking” was used to describe this phenomenon, Washburn predicted the dynamics of penetration of liquids into cylindrical capillaries to follow a diffusion relation where the penetrated distance is proportional to the square root of time.<sup>1</sup> More recently, Bico et al.<sup>2</sup> studied wetting behavior on silicon micropillars and investigated its dynamics by balancing the capillary force that drives liquid into small spaces and the impeding viscous force due to fluid viscosity. Since wicking is defined as the flow of a thin liquid film within the structure that extends from a reservoir of fluid, such as a droplet, this phenomenon is driven by the capillary pressure.

In recent work, engineered nanostructures with different geometrical features have been investigated for wicking dynamics due to their increased surface roughness.<sup>19–22</sup> These include vertical arrays of synthesized nanotubes/nanowires and lithographically patterned nano/microstructured pillars, which demonstrated excellent wicking properties. For example, liquid spreading and wicking on a zircaloy surface with carbon nanotube forests were analyzed by measuring the wicking speed and amount of absorbed water.<sup>21</sup> The wicking dynamics on silicon micro/nanopillars has also been studied

and the wicking enhancement agrees with theoretical prediction models.<sup>22</sup> In these cases nanostructures with high surface roughness increase the ratio of actual surface area to the projected area, and therefore can improve wicking dynamics by increasing the driving capillary pressure. However, finer feature sizes and narrower channels give rise to a larger viscous force, which obstructs the liquid flow. Therefore, nanostructures with high surface roughness do not necessarily lead to better wicking dynamics due to viscous friction effects.<sup>3</sup>

In this work we report on three-dimensional (3D) hierarchical nanopillars with ZnO nanowires to increase surface roughness without obstructing liquid flow. This approach focuses on the balance between these two competing factors, namely capillary action and viscous forces, to achieve better wicking dynamics. The use of hierarchical texture to improve wetting<sup>4–7</sup> and heat transfer<sup>8</sup> has been studied, but wicking in structures with nanoscale roughness approaching the micro-scale channel size has not been studied. The proposed method was centered on the use of a periodic array of silicon nanopillars with 100 nm-scale features for the wicking channels, while smaller ZnO nanowires with 10 nm-scale diameters were synthesized on the substrate surface to increase surface roughness. The hierarchical structure was fabricated using a combination of interference lithography and hydrothermal synthesis, allowing for the independent control of the

Received: May 16, 2016

Revised: July 22, 2016

Published: July 26, 2016

nanopillars and nanowires geometries, respectively. The effects of the nanowire length on the wicking dynamics were examined using experimental testing and theoretical modeling.

## EXPERIMENTAL METHODS

The fabrication process of 3D ZnO hierarchical nanostructures is illustrated in Figure 1. The silicon substrates were spin-coated

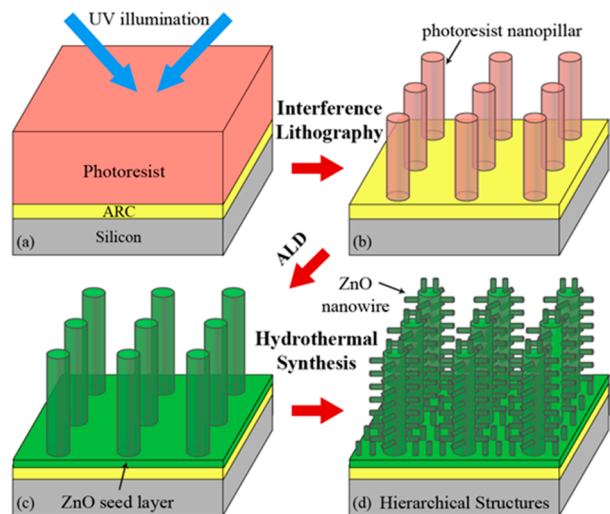


**Figure 1.** Schematic diagram of the fabrication process of ZnO 3D hierarchical nanostructures using a combination of interference lithography, ALD, and hydrothermal synthesis.

sequentially with an antireflection coating (ARC i-CON-16, Brewer Science, Inc.) and a positive photoresist (Sumitomo PFi88A7) with 500 nm thickness. The thickness of the ARC layer was designed to be around 100 nm thick to minimize the reflection from the resist and ARC interface. The samples were exposed using a Lloyd's mirror interference lithography setup<sup>23,24</sup> with a He–Cd laser source ( $\lambda = 325$  nm), as shown in Figure 1(a). The pattern period can be controlled by alternating the interference angle, and two orthogonal exposures were performed to generate a square array of nanopillars with period of 500 nm, as shown in Figure 1(b). The exposure dose ( $\sim 40$  mJ/cm<sup>2</sup>) was controlled by the exposure time, and the exposed photoresist was developed using 2.4% tetramethylammonium hydroxide (TMAH) solution (Microposit MF-CD-26). The pillar

diameter and height can be controlled by the exposure dose and initial resist thickness, respectively. The pattern can also be transferred into the silicon substrate using oxygen and hydrogen bromide (HBr) reactive ion etching (RIE) for more robust structures (see Supporting Information A).

To further increase the surface area, the nanopillars were used as a surface template to grow 1D ZnO nanowires by chemical synthesis. First, the nanopillars were conformally coated with a ZnO seed layer using atomic layer deposition (ALD),<sup>25,26</sup> as shown in Figure 1(c). This was performed in a custom-built hot-wall reactor at 100 °C and pressure of  $\sim 2$  Torr. Diethyl zinc (95%, STREM Chemicals) and deionized water were sequentially dosed to the reactor chamber for 2 s, with 60 s of N<sub>2</sub> purge between the precursor doses. 200 cycles of ALD ZnO ( $\sim 36$  nm thickness) were coated onto the nanostructures before hydrothermal synthesis of ZnO nanowires. ZnO nanowires were then grown using hydrothermal synthesis in an aqueous solution of Zn(NO<sub>3</sub>)<sub>2</sub>•6H<sub>2</sub>O and (CH<sub>2</sub>)<sub>6</sub>N<sub>4</sub> at 80 °C. The thickness of the ZnO ALD layer and the length of nanowires were independently controlled by the number of ALD cycles and the duration of hydrothermal synthesis, respectively. A schematic of the resulting hierarchical structure consisting of ZnO-coated nanopillars and ZnO nanowires is illustrated in Figure 1(d).

To examine the effect of ZnO nanowire length, the same nanopillar geometry was used for different nanowire synthesis times. The key to examining the hierarchical effect was to keep the pillar geometry constant while controlling the nanowire length, which simultaneously increased roughness and reduced channel width. Figure 2 shows scanning electron microscope (SEM, JEOL 6400F) images of ZnO 3D hierarchical nanostructures with 60 nm, 90 nm, 120 and 170 nm nanowire length on 500 nm period pillars. The samples were fabricated under the same conditions except for the duration of hydrothermal synthesis, which gave rise to the difference in ZnO nanowire lengths for different samples. It can be seen from the SEM images that the ZnO nanowires formed perpendicularly on the surface of not only the nanopillars, but also the base of the substrate.

The fabricated hierarchical 3D structures with four different lengths of nanowires were tested for wicking characteristics by placing a droplet of deionized water or ethanol on the sample surface. The droplet penetration processes were recorded using a high-speed camera operating at 100 frames per second. Each individual frame was analyzed to determine the wicking dynamics in different samples and fluids. To understand the wicking dynamics better, a theoretical wicking model examining how the capillary pressure and viscous force are affected by the structural geometry is presented (see Supporting Information B), and the diffusion constant can be derived:

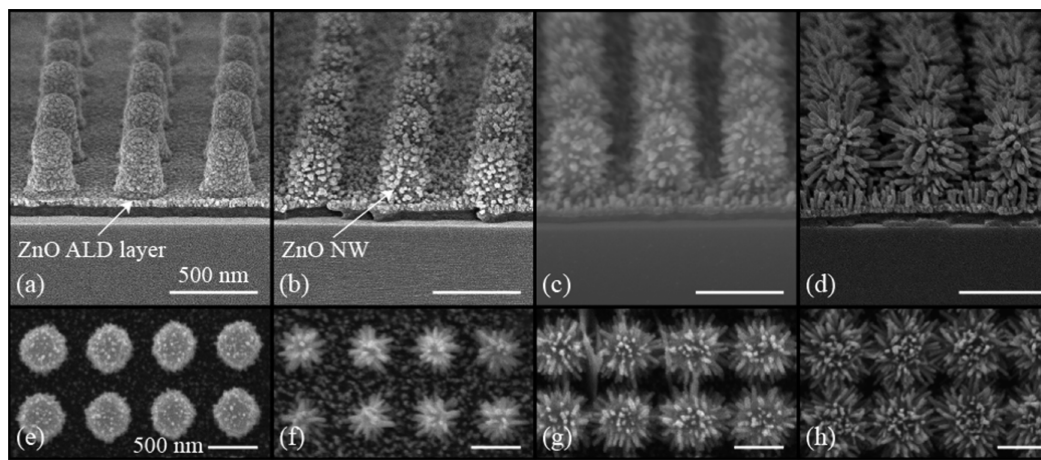


**Figure 2.** SEM images of ZnO 3D hierarchical nanostructures with nanowire length from 0 to 170 nm length. Cross-sectional images of samples with length of (a) 0 nm, (b) 60 nm, (c) 90 nm, and (d) 120 nm. Top-view images of samples with length of (e) 60 nm, (f) 90 nm, (g) 120 nm, and (h) 170 nm.

$$D = \frac{2\gamma h \cos \theta - \cos \theta_c}{3\mu\beta \cos \theta_c} \quad (1)$$

The constant  $D$  (units of  $\text{mm}^2/\text{s}$ ) determines the wicking speed within the structure, where  $\gamma$  is the liquid surface tension,  $\mu$  is the liquid viscosity,  $h$  is the height of the channel,  $\theta$  is the equilibrium liquid contact angle on an ideal flat surface of the same chemical composition,  $\theta_c$  is the critical angle for wicking to occur, and  $\beta$  is a geometric parameter of the nanostructure and nanowires.

## RESULTS AND DISCUSSION

The fabricated hierarchical samples using silicon substrates were experimentally characterized to examine their wicking properties. To examine the hydrophilicity of the nanostructures, the apparent contact angles of water on samples with different lengths of nanowires ( $l$ ) were measured using a goniometer, as shown in Figure 3. The contact angles declines

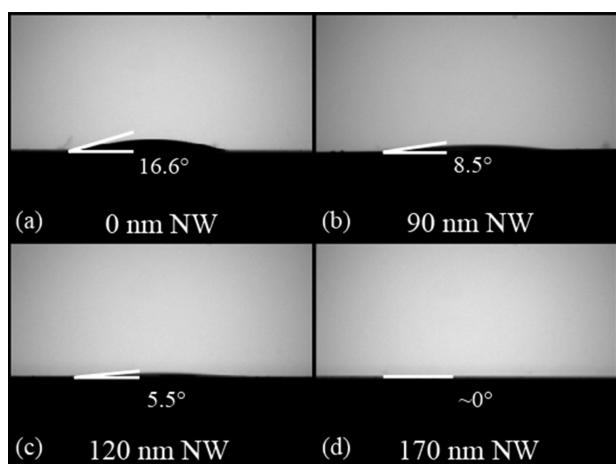


**Figure 3.** Apparent water contact angle of fabricated hierarchical structures with (a) no (b) 90 nm, (c) 120 nm, and (d) 170 nm nanowire length.

continuously with the increase of nanowire lengths and were  $16.6^\circ$ ,  $8.5^\circ$ ,  $5.5^\circ$ , and  $\sim 0^\circ$  for  $l = 0, 90, 120,$  and  $170$  nm, respectively. These results indicate that the hydrophilicity improved as the surface area of hierarchical nanostructures increased, as expected. It is important to note that hydrophilicity of the fabricated nanostructures was not stable due to the high surface energy. The contact angles of all samples were observed to increase with time. This is believed to be due to contaminations from the ambient environment reacting with the structure surface.<sup>27–29</sup> A variety of hydrocarbon compounds from air adsorb onto the sample surfaces, which cause surface contamination and reduced hydrophilicity. To keep the samples free of contamination in order to retain the wicking characteristics, the samples were stored in deionized water before tests. Ultraviolet (UV) illumination and oxygen plasma were also applied to the nanostructures to remove surface contamination, which resulted in improved surface wetting.<sup>30,31</sup>

To examine the wicking dynamics, droplets of water ( $\gamma = 7.28 \times 10^{-2} \text{N/m}$ ,  $\mu = 8.9 \times 10^{-4} \text{Pa}\cdot\text{s}$ ) and ethanol ( $\gamma = 2.24 \times 10^{-2} \text{N/m}$ ,  $\mu = 9.8 \times 10^{-4} \text{Pa}\cdot\text{s}$ ) with a volume of  $1.5 \mu\text{L}$  were dispensed onto samples with five different nanowire lengths ( $l = 0, 60, 90, 120,$  and  $170$  nm) using pipettes. The spreading process was recorded using a high-speed camera (Phantom v4.3 from Vision Research, Inc.), and the snapshots of ethanol wicking on the sample with 170 nm ZnO nanowires are shown

in Figure 4. The droplet spreads quickly and continues the wicking process over more than 20 mm during the initial 30 s.

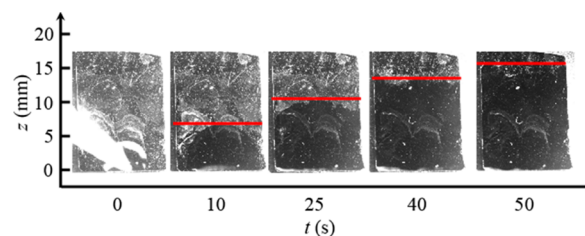


**Figure 4.** Snapshots of ethanol wicking experiments on 3D hierarchical nanostructures. The wicking front is marked by the red dashed lines.

The water and ethanol contact angles on a flat ALD deposited ZnO surface were determined experimentally to be  $\theta_w = 65^\circ$  and  $\theta_c = 10^\circ$ . The fabricated 3D hierarchical nanostructures satisfy the wicking condition for both water and ethanol (see Supporting Information B). In the case of wicking ethanol, the contact angle was very small and there was only one liquid front that could be observed and measured. As for water, it can be observed from the videos that there were two separated liquid fronts (see Supporting Information C). The inner one was the contact front of the water reservoir spreading on top of the structure surface, which marched slower than the outside wicking front marking the liquid penetration into the narrow spaces in the hierarchical nanostructures.

Through analyzing the wicking videos frame by frame, the experimental wicking distance ( $z$ ) traveled by the wicking front was obtained. Since the model indicated that the wicking process follows the diffusion law described in Equation 1, the wicking distance was plotted versus the square root of time for water and ethanol, as shown in Figure 5. It was observed that

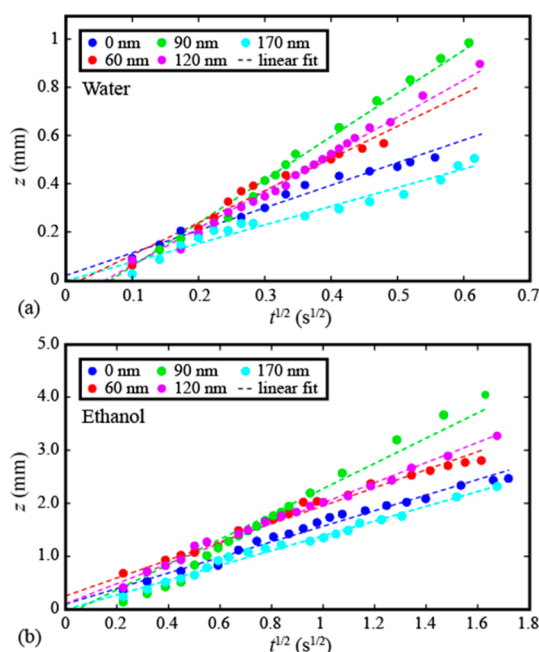


**Figure 5.** Plot of (a) water and (b) ethanol wicking distance  $z$  vs square root of time for 500 nm-period nanopillar structures with nanowire lengths of 0, 60, 90, 120, and 170 nm. The dashed lines are linear fits with corresponding color.

the wicking speed for both liquids improve as the nanowire length is increased from 0 to 90 nm. This trend agrees well with the understanding that increased structure roughness can improve capillary action and wetting, leading to a higher wicking speed. However, the wicking speed decreased when the nanowire length was increased further to 120 and 170 nm, with the latter sample performing even worse than nanopillars without any nanowires. The decrease in wicking speed can be attributed to the increase in viscous forces associated with the narrower wicking channels, which can be visually observed in the SEM images shown in Figure 2(d) and 2(h). Therefore, while longer nanowires can enhance roughness and lower contact angle, they also obstruct flow and limit wicking behaviors. This trend can be observed for both water and ethanol, indicating this wicking behavior is a result of the structure geometry and not fluid properties.

To analyze the data further, a linear fit was applied to all five series of data to determine the diffusion constant  $D$ , which can be calculated to be the square of the slopes (for raw data see Supporting Information C). It can be seen that the plot of experimental data from wicking videos conforms to the linear fit well, demonstrating that the diffusion law could be used to describe the wicking dynamics. Figure 6 compares exper-

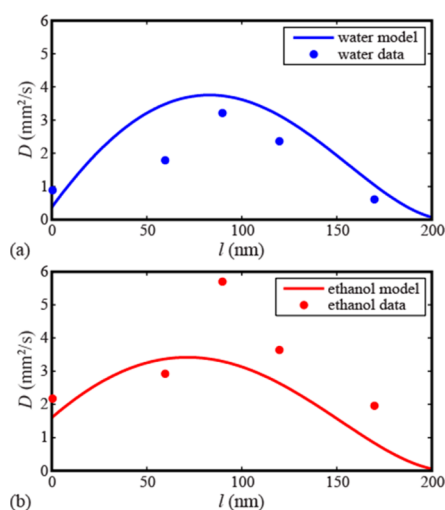


**Figure 6.** Experimental data and theoretical prediction of the diffusion constant  $D$  versus nanowire length  $l$  for (a) water and (b) ethanol.

imentally calculated with theoretical  $D$  derived from the proposed model. Here the model is based on a pillar height of 750 nm, diameter of 180 nm, and spacing of 350 nm with a nanowire diameter of 30 nm (see Supporting Information B). In comparison to nanopillars without any nanowires, the wicking coefficients improve by a factor of 3 for both water and ethanol when the nanowires were 90 nm. It can be observed that the wicking constant  $D$  initially increases with nanowire length, reaching a maximum before decreasing when the nanowires are too long. These results confirm that when the nanowires are relatively short compared with the pillar spacing, the increase in surface roughness leads to faster wicking. However, when the nanowires are long enough so that the wires grown on adjacent nanopillars cross, the fluid flow will be obstructed inside the nanostructures. While there are some differences in the absolute values, the overall data trends for both water and ethanol agree well with the theoretical model. The disagreement in the model may be a result of the

difference in nanowire geometry and density on top, side, and base of the nanopillars, which were assumed to be uniform in the model. As a result the local wetting and wicking might behave differently. The removal of contamination might also be more effective on pillar top surface than the base, leading to nonuniform surface properties that are not included in the model.

These results indicate that the addition of nanoscale nanowires on larger surface structures can improve wicking dynamics, but the improvement is limited by the obstruction of fluid flow for longer nanowires. The key parameter to consider is the spacing between the pillars, which determines the effective channel width in our model. When the nanowire length approaches roughly half of the pillar spacing the channel width is effectively reduced to zero, which limits fluid flow and wicking. The limitation here can be mitigated by using nanopillars with larger spacing, in which case longer nanowire length can be used to further increase surface roughness. The key parameter to consider in the optimization of wicking dynamics in hierarchical nanostructures is the relative length of the nanowires for different pillar spacing.

## CONCLUSION

In this work, we presented the fabrication of 3D ZnO hierarchical nanopillars with nanowires and investigated their wicking properties. We found that the introduction of nanowires can successfully improve the wicking properties of nanopillars by up to a factor of 3, until the wire length approaches half of the pillar spacing and starts to obstruct flow. We also proposed a wicking model based on the balance of capillary and viscous forces, which agrees well with the experimental data collected from the dynamic wicking tests for both water and ethanol. The geometry of the two-tier structures can be independently controlled by interference lithography and hydrothermal synthesis, allowing for the effective control of wicking dynamics. The independent control of parameters is useful in optimizing the nanostructure and nanowire geometry, and exploring other factors for better wicking behavior. The proposed hierarchical nanostructures could be utilized in broad applications for humidity harvesting, microfluidic devices, and integrated heat exchangers.

## ASSOCIATED CONTENT

### Supporting Information

The Supporting Information is available free of charge on the ACS Publications website at DOI: 10.1021/acs.langmuir.6b01864.

Additional information on fluidic model and wicking data. (PDF)

## AUTHOR INFORMATION

### Corresponding Author

\*E-mail: [chichang@ncsu.edu](mailto:chichang@ncsu.edu).

### Notes

The authors declare no competing financial interest.

## ACKNOWLEDGMENTS

This work was performed in part at the NCSU Nanofabrication Facility (NNF) and the Analytical Instrumentation Facility (AIF) at North Carolina State University, which are supported by the State of North Carolina and the National Science Foundation (award number ECCS-1542015). The NNF and

AIF are members of the North Carolina Research Triangle Nanotechnology Network (RTNN), a site in the National Nanotechnology Coordinated Infrastructure (NNCI). This work was supported by a NASA Office of the Chief Technologist's Space Technology Research Opportunity – Early Career Faculty grant (grant NNX12AQ46G) and by the National Science Foundation (grant EEC-1160483) through the Nanosystems Engineering Research Center for Advanced Self-Powered Systems of Integrated Sensors and Technologies (ASSIST).

## REFERENCES

- (1) Washburn, E. W. The Dynamics of Capillary Flow. *Phys. Rev.* **1921**, *17*, 273–283.
- (2) Bico, J.; Tordeux, C.; Quéré, D. Rough Wetting. *Europhys. Lett.* **2001**, *55*, 214–220.
- (3) Quere, D. Wetting and Roughness. *Annu. Rev. Mater. Res.* **2008**, *38*, 71–99.
- (4) Wu, A. H. F.; Cho, K. L.; Liaw, I. I.; Moran, G.; Kirby, N.; Lamb, R. N. Hierarchical Surfaces: An *In Situ* Investigation into Nano and Micro Scale Wettability. *Faraday Discuss.* **2010**, *146*, 223–232.
- (5) Fusi, M.; Di Fonzo, F.; Casari, C. S.; Maccallini, E.; Caruso, T.; Agostino, R. G.; Bottani, C. E.; Li Bassi, A. Island Organization of TiO<sub>2</sub> Hierarchical Nanostructures Induced by Surface Wetting and Drying. *Langmuir* **2011**, *27*, 1935–1941.
- (6) Passoni, L.; Bonvini, G.; Luzio, A.; Facibeni, A.; Bottani, C. E.; Di Fonzo, F. Multiscale Effect of Hierarchical Self-Assembled Nanostructures on Superhydrophobic Surface. *Langmuir* **2014**, *30*, 13581–13587.
- (7) Chu, K.-H.; Joung, Y. S.; Enright, R.; Buie, C. R.; Wang, E. N. Hierarchically Structured Surfaces for Boiling Critical Heat Flux Enhancement. *Appl. Phys. Lett.* **2013**, *102*, 151602.
- (8) Nam, Y.; Sharratt, S.; Byon, C.; Kim, S.-J.; Ju, Y. S. Fabrication and Characterization of the Capillary Performance of Superhydrophilic Cu Micropost Arrays. *J. Microelectromech. Syst.* **2010**, *19*, 581–588.
- (9) Nam, Y.; Sharratt, S.; Cha, G.; Ju, Y. S. Characterization and Modeling of the Heat Transfer Performance of Nanostructured Cu Micropost Wicks. *J. Heat Transfer* **2011**, *133*, 101502.
- (10) Oshman, C.; Li, Q.; Liew, L.-A.; Yang, R.; Lee, Y. C.; Bright, V. M.; Sharar, D. J.; Jankowski, N. R.; Morgan, B. C. Thermal Performance of a Flat Polymer Heat Pipe Heat Spreader Under High Acceleration. *J. Micromech. Microeng.* **2012**, *22*, 045018.
- (11) Koch, K.; Barthlott, W. Superhydrophobic and Superhydrophilic Plant Surfaces: An Inspiration for Biomimetic Materials. *Philos. Trans. R. Soc., A* **2009**, *367*, 1487–1509.
- (12) Andrews, H. G.; Eccles, E. A.; Schofield, W. C. E.; Badyal, J. P. S. Three-Dimensional Hierarchical Structures for Fog Harvesting. *Langmuir* **2011**, *27*, 3798–3802.
- (13) Zhai, L.; Berg, M. C.; Cebeci, F. C.; Kim, Y.; Milwid, J. M.; Rubner, M. F.; Cohen, R. E. Patterned Superhydrophobic Surfaces: Toward a Synthetic Mimic of the Namib Desert Beetle. *Nano Lett.* **2006**, *6*, 1213.
- (14) Cebeci, F. Ç.; Wu, Z.; Zhai, L.; Cohen, R. E.; Rubner, M. F. Nanoporosity-Driven Superhydrophilicity: A Means to Create Multifunctional Antifogging Coatings. *Langmuir* **2006**, *22*, 2856–2862.
- (15) Parker, A. R.; Lawrence, C. R. Water Capture by a Desert Beetle. *Nature* **2001**, *414*, 33–34.
- (16) Guillaume, D. W.; Devries, D. Improving the Pneumatic Nebulizer by Shaping the Discharge of the Capillary Wick. *J. Biomed. Eng.* **1991**, *13*, 526–528.
- (17) Araujo, A. C.; Song, Y.; Lundeberg, J.; Stahl, P. L.; Brumer, H. Activated Paper Surfaces for the Rapid Hybridization of DNA through Capillary Transport. *Anal. Chem.* **2012**, *84*, 3311–3317.
- (18) Ueda, E.; Levkin, P. A. Emerging Applications of Superhydrophilic-Superhydrophobic Micropatterns. *Adv. Mater.* **2013**, *25*, 1234–1247.
- (19) Ishino, C.; Reyssat, M.; Reyssat, E.; Okumura, K.; Quéré, D. Wicking within forests of micropillars. *Europhys. Lett.* **2007**, *79*, 56005.
- (20) Courbin, L.; Bird, J. C.; Reyssat, M.; Stone, H. A. Dynamics of Wetting: From Inertial Spreading to Viscous Imbibition. *J. Phys.: Condens. Matter* **2009**, *21*, 464127.
- (21) Ahn, H. S.; Park, G.; Kim, J.; Kim, M. H. Wicking and Spreading of Water Droplets on Nanotubes. *Langmuir* **2012**, *28*, 2614–2619.
- (22) Mai, T. T.; Lai, C. Q.; Zheng, H.; Balasubramanian, K.; Leong, K. C.; Lee, P. S.; Lee, C.; Choi, W. K. Dynamics of Wicking in Silicon Nanopillars Fabricated with Interference Lithography and Metal-Assisted Chemical Etching. *Langmuir* **2012**, *28*, 11465–11471.
- (23) Bagal, A.; Chang, C.-H. Fabrication of subwavelength periodic nanostructures using liquid immersion Lloyd's mirror interference lithography. *Opt. Lett.* **2013**, *38*, 2531–2534.
- (24) Smith, H. I. Low cost nanolithography with nanoaccuracy. *Phys. E* **2001**, *11*, 104–109.
- (25) Spagnola, J. C.; Gong, B.; Arvidson, S. A.; Jur, J. S.; Khan, S. A.; Parsons, G. N. Surface and sub-surface reactions during low temperature aluminium oxide atomic layer deposition on fiber-forming polymers. *J. Mater. Chem.* **2010**, *20*, 4213–4222.
- (26) Gong, B.; Peng, Q.; Jur, J. S.; Devine, C. K.; Lee, K.; Parsons, G. N. Sequential Vapor Infiltration of Metal Oxides into Sacrificial Polyester Fibers: Shape Replication and Controlled Porosity of Microporous/Mesoporous Oxide Monoliths. *Chem. Mater.* **2011**, *23*, 3476–3485.
- (27) Lundgren, M.; Allan, N. L.; Cosgrove, T.; George, N. Wetting of Water and Water/Ethanol Droplets on a Non-Polar Surface: A Molecular Dynamics Study. *Langmuir* **2002**, *18*, 10462–10466.
- (28) Meng, X. Q.; Zhao, D. X.; Zhang, J. Y.; Shen, D. Z.; Lu, Y. M.; Dong, L.; Xiao, Z. Y.; Liu, Y. C.; Fan, X. W. Wettability Conversion on ZnO Nanowire Arrays Surface Modified by Oxygen Plasma Treatment and Annealing. *Chem. Phys. Lett.* **2005**, *413*, 450–453.
- (29) Lifton, V. A.; Simon, S. Preparation and Electrowetting Transitions on Superhydrophobic/ Hydrophilic Bi-Layer Structures. *J. Porous Mater.* **2011**, *18*, 535–544.
- (30) Drelich, J.; Chibowski, E.; Meng, D. D.; Terpilowski, K. Hydrophilic and Superhydrophilic Surfaces and Materials. *Soft Matter* **2011**, *7*, 9804.
- (31) Liu, H.; Feng, L.; Zhai, J.; Jiang, L.; Zhu, D. Reversible Wettability of a Chemical Vapor Deposition Prepared ZnO Film between Superhydrophobicity and Superhydrophilicity. *Langmuir* **2004**, *20*, 5659–5661.